Influence of textural characteristics and mineral composition on the acoustic behavior under acoustic integrated uniaxial compression

Kun Du[1] · Xinyao Luo[1] · Tao Zhou[2]

Abstract

This paper presents acoustic integrated uniaxial compression tests on 11 types of rock specimens to investigate their acoustic behavior and brittleness properties. Thin section analysis was used to characterize the mineral composition and structural characteristics of the rocks, and their grain uniformity was quantified using the weighted variable coefficient. The acoustic signals of the 11 types of rock specimens during uniaxial compression were monitored and recorded in real time using ultrasonic and acoustic emission (AE) testing technologies. The relationships between grain characteristics, mineral composition, and acoustic behaviors were investigated. The results showed that the centroid frequency (F_{cf}) and transmission coefficient (T_{cf}) of the rocks were generally positively correlated with grain uniformity, and mineral grain size had different effects on igneous and sedimentary rocks. The ultrasonic (V_p, F_{cf}, T_{cf}) and damage (D_3) characteristics were significantly influenced by the three main mineral compositions (quartz, plagioclase, and k-feldspar). Additionally, differences in the percentage growth of F_{cf} and T_{cf} in igneous, sedimentary, and metamorphic rocks were explored and attributed to differences in the structural construction and abundance of initial microcracks. A novel brittleness index for rocks was established based on the ultrasonic characteristic parameters and mineral composition, and the existing brittleness index based on AE parameters was improved.

Keywords Ultrasonic · Lithology · Wave velocity · Mineral composition · Particle size · Brittleness index

Introduction

Rocks, as the foundation of underground engineering, are characterized by varying degrees of porosity and microcracks that result from differences in lithology and stress state. Under external loads and environmental conditions, these microdefects can propagate and coalesce, resulting in macroscopic rock deformation (Liu et al. 2019; Zhou et al. 2022). The progressive failure of rocks due to crack propagation is a crucial factor in determining the stability and sustainable utilization of rock structures. Therefore, it is essential to study the microcracking and deformation behavior of rocks from a microscopic perspective.

In the past decades, numerous scholars have studied the microscopic characteristics and microcrack extension behavior of rocks by microscopic observation techniques such as acoustic measurements (AE technology and ultrasonic testing technology), scanning electron microscopy (Li et al. 2011; Zhou et al. 2023), X-ray computed tomography (CT) (Bam et al. 2020), and nuclear magnetic resonance imaging (Gingras et al. 2002; Zhang et al. 2022). Acoustic measurements have the advantages of convenient operation, real-time monitoring, and nondestructive measurement, so they are widely used in laboratory tests. In terms of AE technology, the progressive damage process of rocks has been studied using characteristic parameters, such as AE ringing counts (Wang et al. 2022), AE energy (Du et al. 2021), AE counts, and the damage differences of different rocks have been found (Tang et al. 2021; Zhao et al. 2021, 2023). In terms of ultrasonic testing technology, the propagation characteristics of ultrasonic waves in rocks under uniaxial compression have been studied extensively (Lian et al. 2019; Greenfield and Graham 1996; Wu et al. 2021), and

✉ Tao Zhou
  tzhou@szu.edu.cn

1   School of Resources and Safety Engineering, Central South University, Changsha, China

2   Guangdong Provincial Key Laboratory of Deep Earth Sciences and Geothermal Energy Exploitation and Utilization, Institute of Deep Earth Sciences and Green Energy, College of Civil and Transportation Engineering, Shenzhen University, Shenzhen, China

the evolution of elastic wave velocity has been investigated mainly by changing cyclic loading conditions (Yang et al. 2020a), loading methods (Sayers 1995), and rock types (Atici 2010; Shirole et al. 2018). Furthermore, in order to study the influence of rock joints, fillers, seepage (Yang et al. 2019, 2020b) on elastic wave propagation and attenuation, some scholars have performed quantitative analysis by using the anisotropy coefficient, attenuation coefficient, quality factor, and other parameters. The above results indicate that the acoustic characteristic parameters of rocks are closely related to the internal microstructure of rocks.

Due to differences in diagenesis and tectonics, the internal microstructure of rocks changes significantly during their formation (Meng et al. 2002), such as mineral composition, textural characteristics (i.e., grain size, distribution and shape), structural construction, microcracks, and porosity (Ozcelik et al. 2013; Wang et al. 2020). Many scholars have studied the mechanical properties and ultrasonic characteristics of rocks from a microscopic perspective. Yao et al. (2020) studied the microstructure, mineral composition, and cementation type of 16 sandstones, and found that strength, modulus, cohesion, and friction coefficient increased with increasing quartz content and grain contact, while decreased with increasing plagioclase and clay mineral content. Wong et al. (2018) investigated the effect of quartz content in igneous rocks on rock strength and related microcracking behavior using PFC^{2D} software, and discussed the effect of mineral distribution on mechanical properties. Ajalloeian et al. (2020) measured ultrasonic pulse velocity and dynamic elastic constants in 10 granites with different lithological characteristics and found that wave velocity and elastic modulus were negatively correlated with grain size, but positively correlated with quartz content. Additionally, Mayr and Burkhardt (2006) and Li et al. (2018) studied the influence of porosity on ultrasonic characteristics and concluded that the wave velocity of rocks decreased with increasing porosity.

Researchers have noted that structural characteristics have a greater impact on rock performance than mineral composition. Merriam et al. (1970) discovered that the tensile strength of California granites is inversely proportional to quartz content, and this phenomenon was attributed to structural differences. Skurtveit et al. (2013) conducted compression tests on poorly lithified sandstones with varying grain sizes, and they attributed the increase in P-wave velocity during the compaction stage to grain rearrangement. Di Martino et al. (2021) characterized the volcanic samples in terms of texture and mineralogy, and established their relationship with coda attenuation measurements. Liu et al. (2020a, b) determined the small strain shear modulus (G_{max}) using shear wave velocity and investigated the relationship between grains uniformity and G_{max}. From these studies, it is evident that intrinsic factors, such as mineral composition,

grain size, and structural connection and distribution characteristics, contribute to differences in the acoustic signal characteristics of rocks.

While a multitude of studies have investigated the propagation characteristics of acoustic signals in rocks, few have examined the impact of lithology on acoustic properties from a microscopic perspective, particularly with regard to ultrasonic spectral characteristics. In this study, uniaxial compression tests, ultrasonic propagation tests, and acoustic emission tests were performed on 11 different types of rock specimens. Fast Fourier variation (FFT) of ultrasonic waveforms was performed and the relationship between damage properties, acoustic spectral characteristics and mineral composition, grains uniformity, and grain size was analyzed. Based on the ultrasonic characteristic parameters and mineral composition, a novel brittleness evaluation index which can evaluate different lithology rocks was established.

Experimental methodology

Specimen preparation

In this study, eleven kinds of rock specimens including sandstone, marble, limestone, andesite, and granite were adopted to prepare the ISRM recommended standard rock specimens for uniaxial compressive test, as shown in Fig. 1. The nominal dimensions of rock specimens were 50 mm in diameter and 100 mm in length. Prior to testing, all rock specimens were ground and polished to ensure a surface roughness of less than 0.02 mm. Table 1 presents the geometric parameters and physical properties of all rock specimens.

Petrographic descriptions

In order to better understand the lithological differences between different rocks, mineral compositions and grain size dimensions of 11 types of rocks were obtained by experiment of rock thin section identification. In the rock thin section identification test, 4 thin sections are selected from different parts of each rock, i.e., 2 perpendicular to the core plane (VCP) and 2 parallel to the core plane (PCP). Figure 2 presents the percentages of rock mineral compositions.

From Fig. 2, it can be observed that with the exception of N-M and N-L, which are primarily composed of calcite (accounting for 98% and 70%, respectively), the other rocks consist mainly of plagioclase, quartz, and K-feldspar. The total percentages of these three minerals are 49% for N-A, 81% for N-G, 72% for N-G, 64% for S-R, 78% for S-W, 89% for S-Y, 53% for S-G, 77% for S-B, and 63% for S-P.

The microstructural images of four typical rocks are presented in Fig. 3. The structural characteristics, mineralogical composition, and rock types of 11 different rocks were

Fig. 1 Rock specimens used in this study

S-Y   S-W   S-B   S-R   S-G

S-P   N-M   N-L   N-A   N-G   N-C
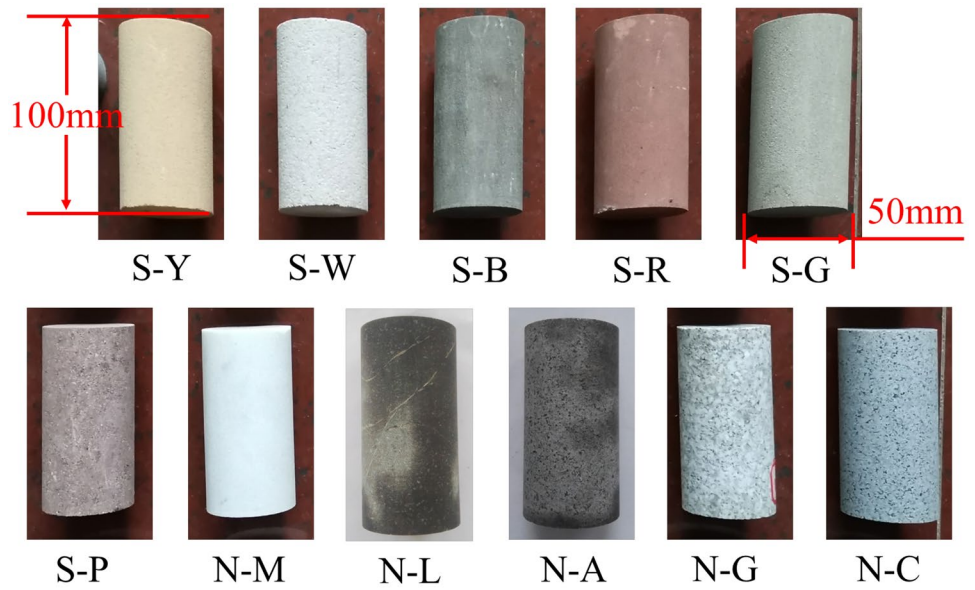
summarized by observing their lithofacies. The grain uniformity of each rock type was quantified using the weighted variable coefficient of Eqs. (1)–(3), as presented in Table 2.
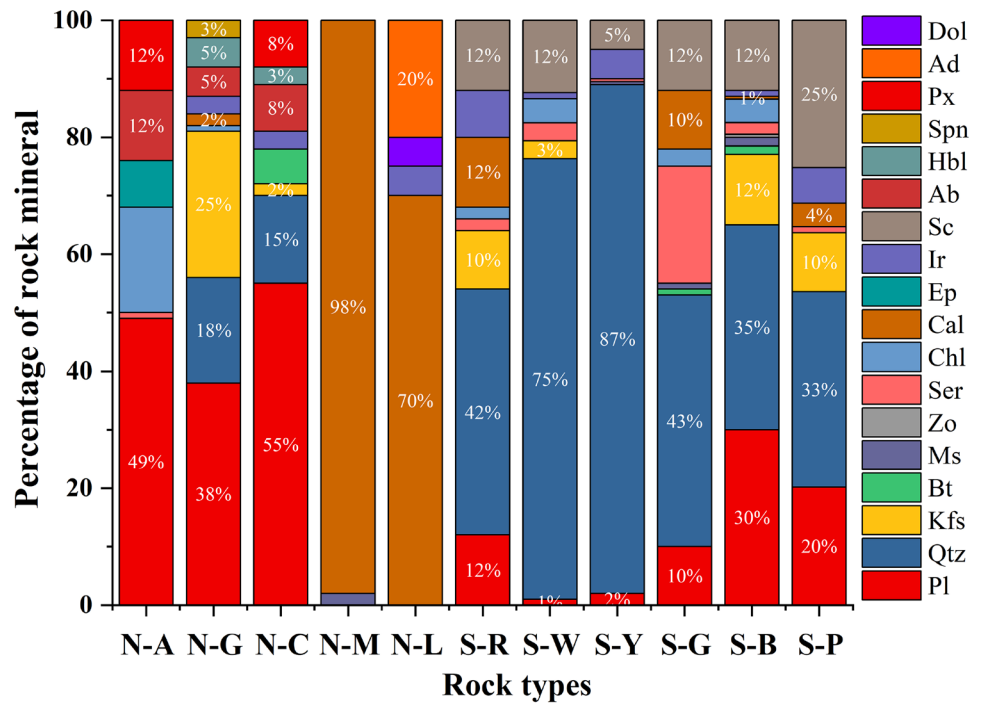
$$WCV = \sum_i W_i \cdot CV_i \tag{1}$$

Table 1 Geometrical, physical, and mechanical properties of different rock specimens

Rock type	Categories lithology	Specimen no.	V_P (m/s)	ρ (g/cm^3)	E (GPa)	v	UCS (MPa)
Altai mountains · andesite	Igneous	N-A-1	6373.36	2.83	24.05	0.21	193.44
		N-A-2	6392.77	2.85	36.22	0.22	222.17
MiLuo · granite		N-G-1	4107.58	2.64	18.20	0.25	110.54
		N-G-2	4337.18	2.30	22.26	0.22	118.25
LeiZhou · granite		N-C-1	5265.93	2.79	24.70	0.17	124.69
		N-C-2	5548.90	2.57	60.14	0.22	160.27
LeiYang · marble	Metamorphic	N-M-1	4028.14	2.69	15.67	0.16	64.71
		N-M-2	4201.49	2.75	20.53	0.19	57.75
HeZhou · limestone		N-L-1	5396.17	2.69	12.61	0.46	44.74
	Sedimentary	N-L-2	6037.95	2.68	37.62	—	115.72
WuDing · red sandstone		S-R-1	3003.55	2.40	10.89	0.19	74.97
		S-R-2	3293.89	2.38	8.96	0.23	80.05
ZiGong · white sandstone		S-W-1	2668.22	2.33	7.27	0.19	36.87
		S-W-2	2640.84	2.34	7.84	0.24	40.21
YunNan · yellow sandstone		S-Y-1	1705.4	2.08	8.05	0.32	46.59
		S-Y-2	1679.53	2.11	8.73	0.46	44.96
ZiGong · gray sandstone		S-G-1	3849.56	2.58	12.11	0.12	76.75
		S-G-2	3834.35	2.60	18.19	0.21	74.00
LongChang · blue sandstone		S-B-1	3286.11	2.31	10.89	0.20	69.14
		S-B-2	3297.71	2.32	12.36	0.23	64.97
JuNan · purple sandstone		S-P-1	3264.39	2.41	14.98	0.13	92.80
		S-P-2	3293.89	2.42	16.96	0.21	93.98

H Length, *D* diameter, ρ density, *E* elasticity modulus, *v* Poisson ratio, V_P P-wave velocity, *UCS* uniaxial compression strength, "—" represents data loss

Fig. 2 Mineral percentage of rocks

where *WCV* is the weighted variable coefficient of grain size, W_i is the content of "mineral *i*," and CV_i is the variable coefficient of the size of "mineral *i*." By identifying thin sections of rocks, 4 groups of mineral grain sizes are summarized, i.e., coarse grains (2.0–0.5 mm), medium grains (0.5–0.25 mm), fine grains (0.25–0.05 mm), and silty sand (0.05–0.005 mm). W_i^j is the mineral content in group *j* of

$$CV_i = \sqrt{\sum_{j=1}^{4} W_i^j \cdot (\bar{S}_j - \bar{x}_i)^2 / W_i} \Bigg/ \bar{x}_i \qquad (2)$$

$$\bar{x}_i = \sum_{j=1}^{4} \bar{S}_j W_i^j / W_i \qquad (3)$$

Fig. 3 Microphotographs of four typical rocks: **a** N-A; **b** N–C; **c** N-M; **d** S-W
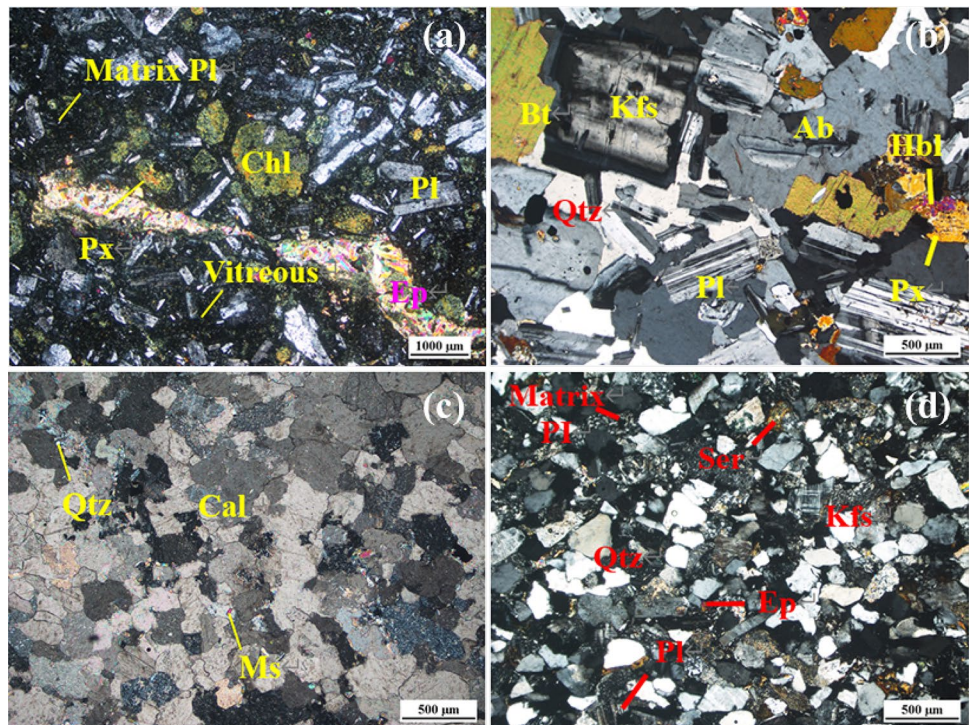
Table 2 Mineralogical and petrographic characteristics of 11 kinds of rocks

Specimen no.	Texture	Major mineral composition (%)	Rock name	Uniformity of grains
N-A	Porphyritic structure, matrix with intersertal texture, massive structure	Pl (50), Px (15), Ep (10), Chl (15),	Melaphyre	0.70
N-G	Semi-dimorphic-orthomorphic granular texture, massive structure	Pl (38), Kfs (25), Ab (10), Qtz (18), Hbl (5)	Biotite pyroxene quartz diorite	0.65
N-C	Semi-dimorphic-orthomorphic granular texture, massive structure	Pl (55), Kfs (2), Ab (8), Qtz (15), Px (8), Hbl (3), Bt (6)	Amphibole-bearing monzogranite	0.51
N-M	Micro-fine grain crystal structure, massive structure	Cal (98), Dol, Ser (2)	Marble	0.47
N-L	Sparry structure cemented algal micrite structure, massive structure. Local fissures developed in the rocks are filled with calcite and iron argillaceous, forming the structure features of veins or microsuture lines	Cal (90), Dol (4)	Cloudy algae limestone	1.30
S-R	Sand-containing powder-fine sand structure, particle support, porous cementation, massive structure	Sc (12), Pl (12), Kfs (10), Qtz (42), Cal (12)	Lithic feldspar quartz sandstone	0.47
S-W	Medium-fine sand structure of argillaceous arenes, porous cementation, massive structure	Sc (15), Pl, Kfs (4), Qtz (73)	Lithic quartz sandstone	0.77
S-Y	Pelitic arenaceous clastic fine sand structure, porous cementation, massive structure	Sc (5), Pl, (2), Qtz (87)	Argillaceous lithic quartz sandstone	0.2
S-G	Sand-containing pelitic medium-fine sand structure, basal cementation, massive structure	Pl (10), Qtz (43), Cal (10)	Lithic calcareous argillaceous sandstone	0.34
S-B	Medium-fine muddy sand structure, massive structure	Sc (12), Pl (30), Kfs (12), Qtz (35)	Tuffaceous lithic feldspar quartz sandstone	0.71
S-P	Coarse-medium sand structure, granular support, porous cementation, massive structure	Sc (25), Pl (20), Kfs (10), Qtz (33)	Lithic feldspar quartz sandstone	0.34

Pl plagioclase, *Qtz* quartz, *Kfs* K-feldspar, *Bt* biotite, *Ms* muscovite, *Zo* zoisite, *Ser* sericite, *Chl* chlorite, *Cal* calcite, *Ep* epidote, *Ir* iron, *Sc* sand chips, *Ab* albite, *Hbl* hornblende, *Spn* sphene, *Px* pyroxene, *Ad* algo detrinite, *Dol* dolomite

"mineral *i*," $\overline{S}_j$ is the average grain sizes of group *j*, and $\overline{x}_i$ represents the average grain size of "mineral *i*." The smaller *WCV* is, the more uniform the grains are, indicating that the rock is closer to equigranular texture.

Experimental equipment and procedures

In this test, the MTS 647 electrohydraulic servo control system with a load range of ± 500 kN and a load accuracy of $\pm 0.5\%$ was utilized, as illustrated in Fig. 4a. The specimens were loaded under the displacement-controlled mode with a loading rate of 0.075 mm/s. The AE activities of the rock specimens were detected and recorded using the PCI-2 AE data-collecting system throughout the loading process. The AE preamplifier was set to 40 dB, and the signal acquisition rate and the sampling threshold were set to 1.0 MHz and 40 dB, respectively. To perform ultrasonic

wave propagation tests, an Olympus 5077PR square wave pulser, a 2012B Tektronix digital phosphor oscilloscope, and a pair of wave transducers with a centre frequency of 1.0 MHz were employed (Zhou et al. 2023). The transducers were placed in the anvils at the ends of the test setup, as shown in Fig. 4b.

The test loading procedures for each rock sample are shown in Fig. 4c. At a uniaxial compression rate of 0.075 mm/s, the pressure on the rock specimen was increased by 5 kN with a pause of 10 s, and the ultrasonic data-collecting device was used to record the waveform generated under the stress state. The procedure was repeated afterward. During the entire procedure, the AE data-collecting equipment monitored the loading in real time until the emergence of a large AE signal was detected, and a large sound from the compressed specimen can clearly be heard. Then, the waveform generated

Fig. 4 Experimental equipment and procedures: **a** MTS 322 electrohydraulic servo control system; **b** experimental equipment for P-wave propagation measurement and acoustic emission detection; **c** test loading procedures
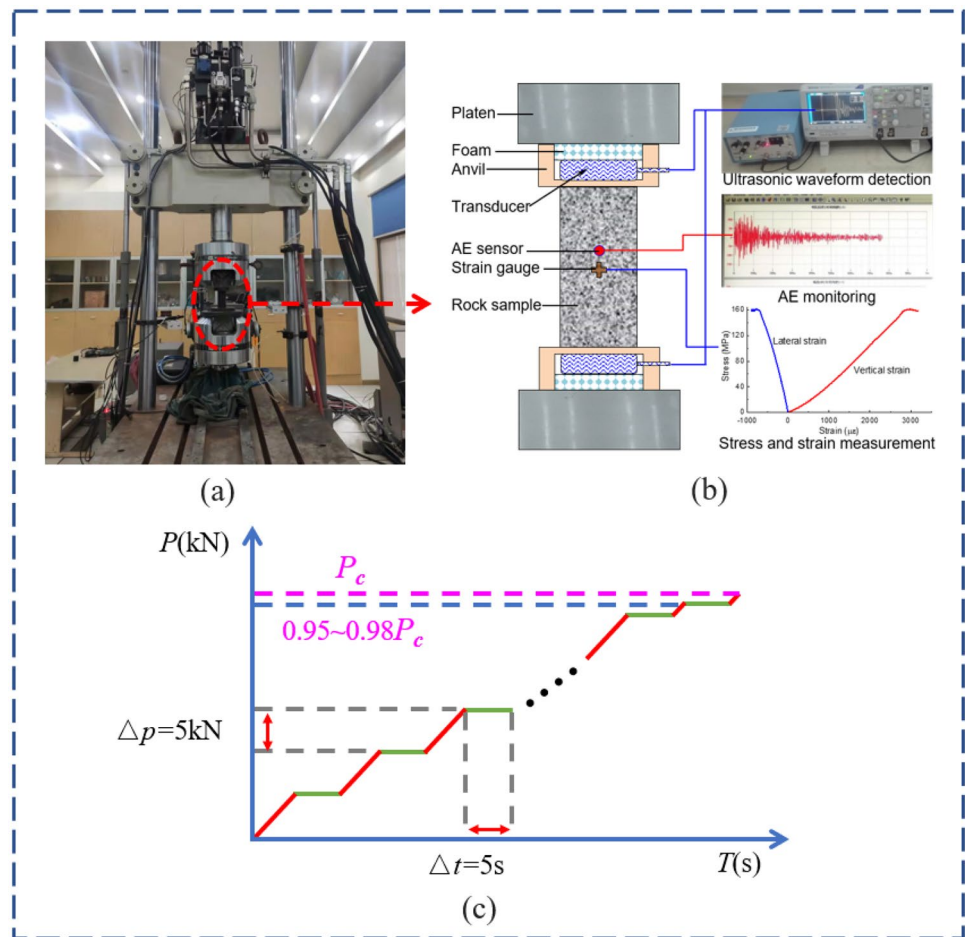
at this point was recorded. At this time, the load level was approximately 0.95–0.98 peak load (P_c), after which the loading was continued until the specimen was destroyed.

Data analysis method

Calculation method of VP

Wave velocity is one of the most important acoustic characteristics and an important index that indirectly reflects the integrity of rock. In order to obtain the wave velocity of each rock sample, it is necessary to calculate the first arrival time of the initial waveform. The arrival time of initial waveforms of two typical samples is given in Fig. 5. The calculation formula of p-wave velocity is as follows:

$$V_P = \frac{H}{T - T_0} \tag{4}$$

where V_P is P-wave velocity, H is the length of the rock specimen, T is the time measured by the transducer when two anvils are attached to the rock specimen, and T_0 is the time measured by the transducer when two anvils are fitted together.

Window selection of fast fourier transform (FFT)

In order to conduct a comprehensive analysis of the wave propagation and attenuation characteristics of different rocks, it is necessary to convert the waveforms from the time domain to the frequency domain. However, the transmitted waveform comprised the initial arrival wave and the subsequent pulse waveform reflected at the interface between the rock specimen and various instruments. To isolate the first arriving pulse from the complete transmitted waveform, a suitable window function needs to be applied to taper the waveforms. The selected taper should extract the initial pulse from the complete waveform
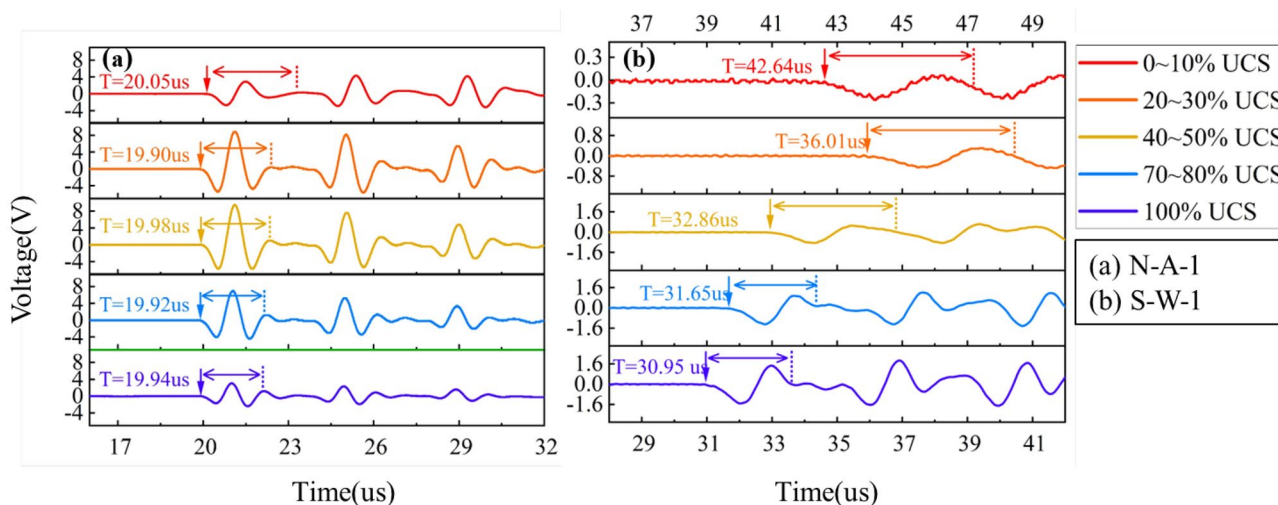
Fig. 5 Examples of waveforms and arrival times for two typical rock samples

without changing the original transmission spectrum while preserving more low-frequency content in the high-frequency range to prevent excessive signal distortion, as recommended by previous studies (Pyrak-Nolte et al. 1990; Yang et al. 2020a, b). Figure 6 shows two examples of the selected transmitted waveforms, where a half-cosine taper with a 2.68 μs window was applied to the waveform of N-A under a loading percentage of 14.53% UCS (28.05 MPa), and a half-cosine taper with a 2.94 μs window was applied to the waveform of S-W under a loading percentage of 95.59% UCS (35.17 MPa).

The window time of the taper function of all rock samples is listed in Table 3. After obtaining all the tapered initial

arrival waves, FFT is performed to obtain the wave spectrum and the typical spectrum obtained is shown in Fig. 7.

Results and analysis

Effects of loading percentage and lithology on VP

The mineral composition and structural characteristics of different rocks lead to variations in their UCS values, resulting in differences in V_P generated by the rocks. Figure 8 depicts that V_P of rock specimens increases rapidly in a nonlinear manner under the loading percentage of 0–20%
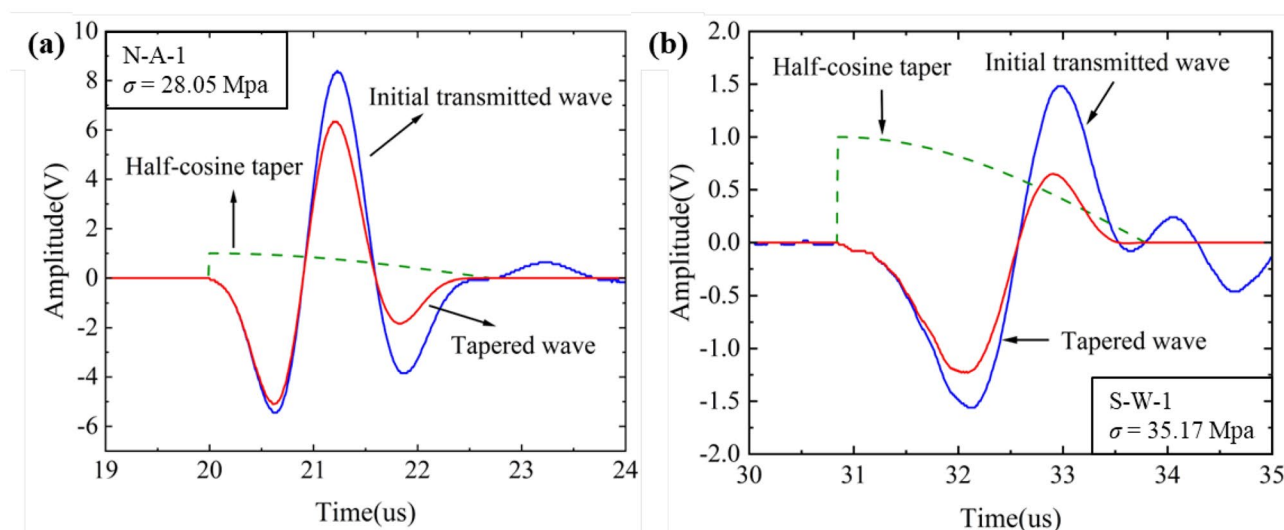

Fig. 6 Signal processing of transmitted waves by half-cosine taper: **a** 2.68us half-cosine taper applied to N-A-1; **b** 2.94us half-cosine taper applied to S-W-1

Table 3 Window time of half-cosine taper for different rock specimens

Igneous and metamorphic rocks	Specimen No.	N-A	N-G	N-A	N-M		N-L
	Window time (µs)	2.68	3.94	2.93	3.06		1.87
Sedimentary rocks	Specimen No.	S-R	S-W	S-Y	S-G	S-B	S-P
	Window time (µs)	3.37	2.94	3.18	3.23	4.04	4.05

UCS. Sedimentary rocks generally show a higher increase in wave velocity than igneous and metamorphic rocks. This phenomenon can be attributed to the difference in the initial microfracture closure degree in the rock. The presence of more initial microcracks in the rock and more crack closure events leads to a more significant increase in V_P. In the subsequent loading process, V_P grows slowly, and the compression of the rock matrix mainly occurs. Since the longitudinal wave velocity is measured in the direction parallel to the stress loading, the longitudinal tensile crack generated in the rock at the late loading stage does not significantly weaken the V_P.

Damage stages of different rocks

To analyze the damage properties of rocks and obtain the relationship between damage evolution and loading percentage of different samples in uniaxial compression, the damage process was quantitatively analyzed by using accumulative AE counts in the following formula:

$$D = \frac{N_S}{N} \tag{5}$$

where D is the damage variable of the rock sample, N_S is the cumulative AE count generated when the rock sample is loaded to a certain level, and N is the total accumulative AE counts generated when the rock sample is loaded to the UCS.

Before macroscopic failure occurs, rocks successively go through 4 different damage stages, i.e., compaction stage, elastic stage, crack stable growth stage, and crack unstable growth stage. These 4 stages can be divided by dividing the time when the acoustic emission count rate, acoustic emission energy, and D suddenly increase. Figure 9 shows the percentages of the 4 stages in 11 rock specimens and the D-value of each stage boundary. Although stage I (compaction stage) and stage II (elastic stage) account for a large proportion of the entire loading process, they play a small role in promoting the increase in the D-value, and the increase in the D-value mainly occurs in stages III (crack stable growth stage) and IV (crack unstable growth stage), which account for a relatively small proportion. The results show that the crack propagation in the rock occurs rapidly during stage III and stage IV, and the crack propagation is more intense during stage IV, and it means the crack growth changes from stable to unstable. Therefore, the damage value (D_3) at the demarcation points of stages III and IV can be used as a basis for judging the imminent failure of the rock.

Effect of grain size on acoustic properties

In order to investigate the spectral variation pattern of different rocks during loading, the centroid frequency (F_{cf}) and transmission coefficient (T_{cf}) (Nakagawa et al. 2000; Quan and Harris 1997) were used in this study to characterize the
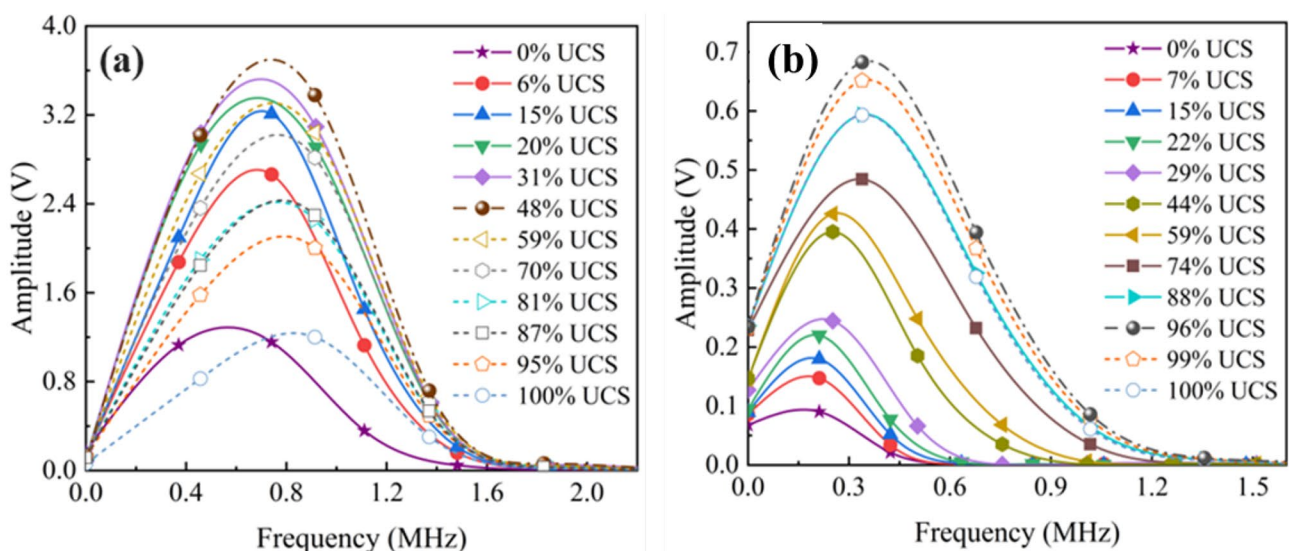

Fig. 7 Spectra of transmitted waves from **a** N-A and **b** S-W under different loading percentages
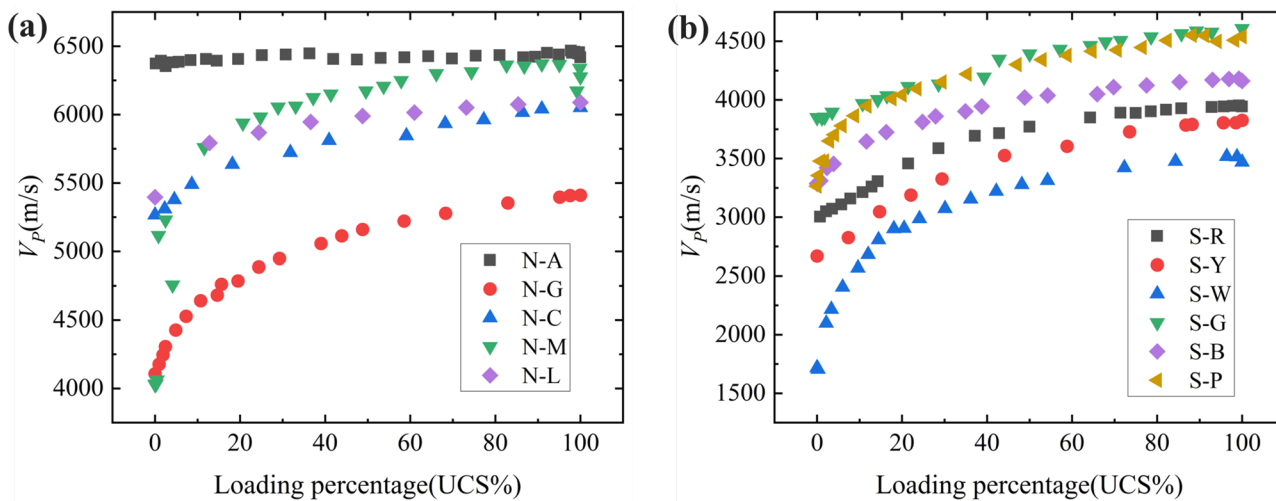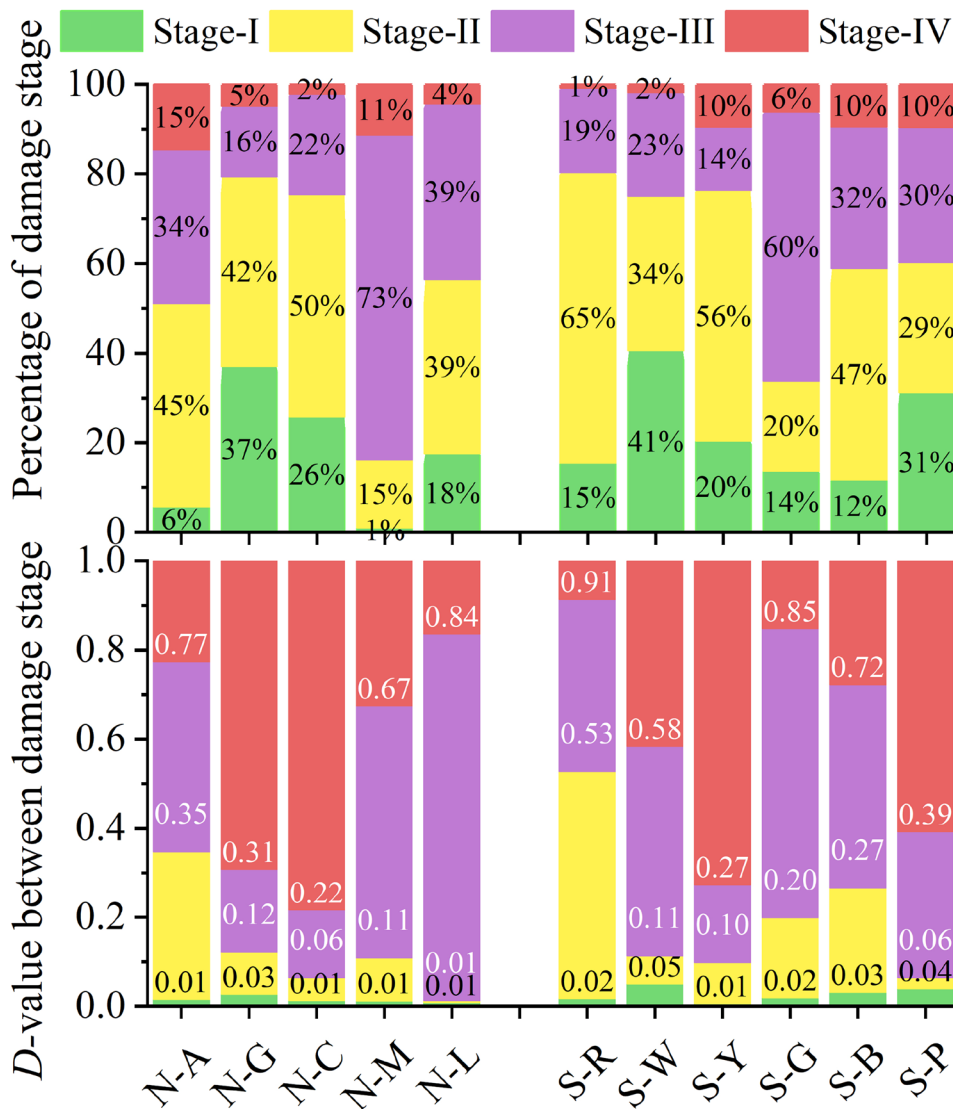
Fig. 8 The variation law of V_P during loading: **a** igneous and metamorphic rocks; **b** sedimentary rocks

Fig. 9 The percentage of damage stage and the distribution of D-value for different rock specimens

spectral signal generated at each stress level, and the definitions are as follows:

$$F_{cf} = \frac{\int_0^\infty f S(f) df}{\int_0^\infty S(f) df} \tag{6}$$

$$T_{cf} = \frac{A_i}{A_0} \tag{7}$$

where F_{cf} and T_{cf} are the centroid frequency and transmission coefficient, respectively; f is the frequency; $S(f)$ is the spectral function; A_0 is the maximum amplitude of the spectrum of the rock specimen before compression; and A_i is the maximum amplitude of the spectrum measured when the loading stops for the ith time in the process of compression.

Figure 10 shows the relationship between F_{cf}, T_{cf} and uniformity of grain under different loading percentages. It is evident that F_{cf}, T_{cf}, and grain uniformity exhibit a positive correlation in sedimentary rocks, meaning that the rock's F_{cf} and T_{cf} increase with decreasing grain uniformity. However, this positive correlation decreases with an increase in loading. In igneous and metamorphic rocks, the positive correlation between F_{cf} and grain uniformity is not significant, which can be attributed to the considerable variations in other lithological factors. The frequency of most rock samples rises with the increase in loading percentage, which is satisfactorily explained by the Doppler effect. The reason behind the decrease in T_{cf} with a reduction in grain homogeneity is that, in the case of uneven grain structures, the acoustic wave gets scattered and refracted at the contact surface of the grains with varying areas, causing attenuation of the acoustic energy, and thus leading to a decrease
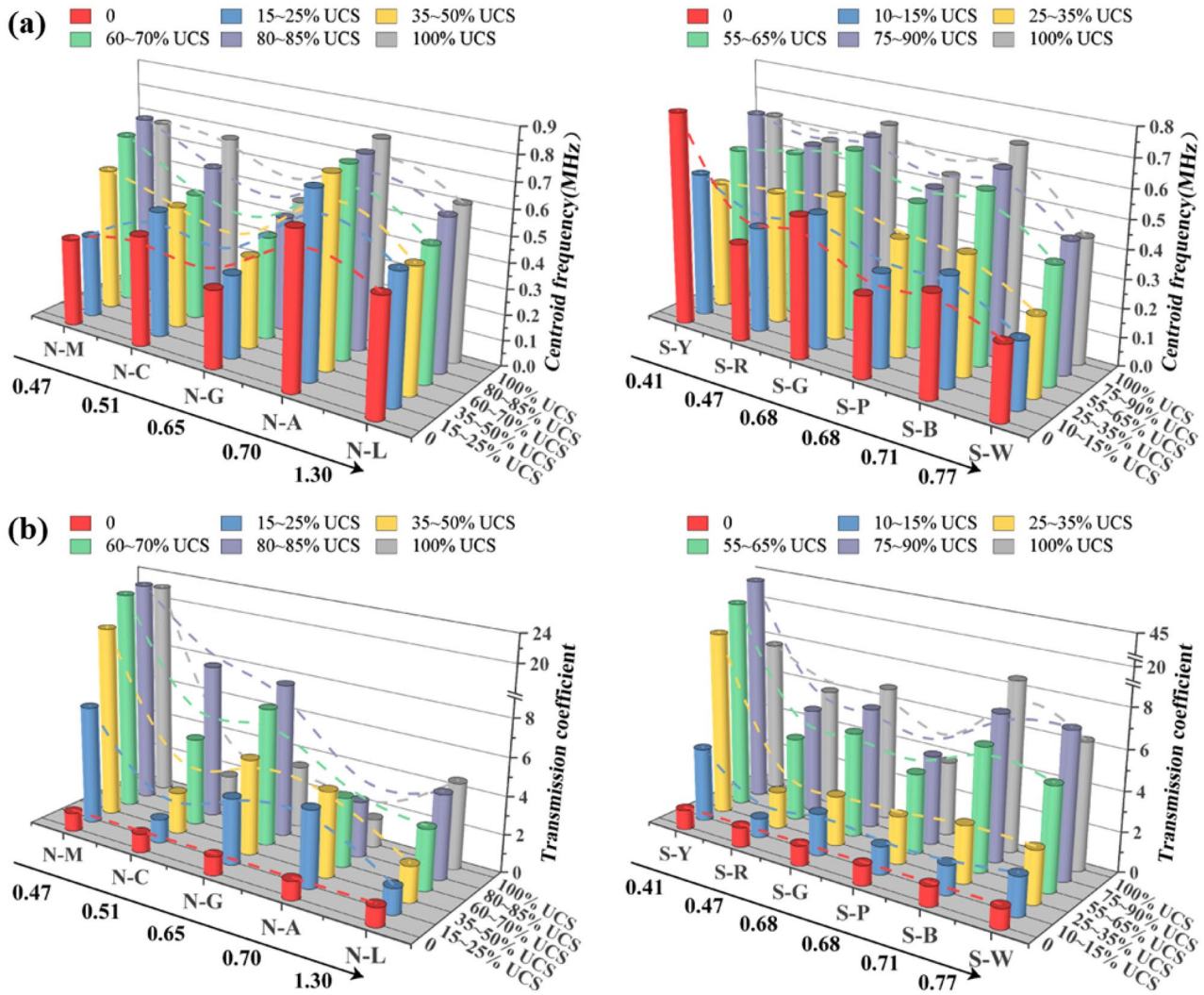

Fig. 10 Relationship between F_{cf}, T_{cf}, and uniformity of grain size under different loading percentages: **a** evolution of F_{cf}; **b** evolution of T_{cf}

in T_{cf}. Therefore, F_{cf} and T_{cf} can be used to some extent as indicators of rock compactness and elastic wave transfer efficiency, respectively.

The maximum grain size in mineral grains can be used as a typical value of rock size (Du et al. 2022; Prikryl et al. 2003), so the distribution statistics of the maximum grain size of three igneous and six sedimentary rocks were plotted. The relationship between the maximum grain size of the three mineral compositions and F_{cf}, T_{cf}, V_P, D_3 is displayed in Fig. 11. The results show that the grain sizes in igneous rocks are much larger than those in sedimentary rocks, especially those of K-feldspar. In igneous rocks, F_{cf} and V_P are negatively correlated with the grain size of the major minerals, while T_{cf} is positively correlated with the grain size. N-A produces a larger D_3 than N-G and N–C, which may be the result of the interaction of other mineral components. In sedimentary rocks, F_{cf} increases with grain size of the major minerals, while T_{cf} and D_3 decrease with grain size of the major minerals. The correlation between V_P and grain size is not significant. It is noteworthy that T_{cf} and D_3 vary almost synchronously with the grain size, and their relationship with the mineral composition is also

synergistic, which indicates that T_{cf} can be used to characterize the degree of rock damage.

The maximum grain size of mineral grains is often used as a representative value of rock size (Du et al. 2022; Prikryl et al. 2003). Therefore, the distribution statistics of the maximum grain size of three igneous and six sedimentary rocks were plotted to investigate their relationship with F_{cf}, T_{cf}, V_P, and D_3. As shown in Fig. 11, the maximum grain sizes in igneous rocks are generally larger than those in sedimentary rocks, particularly in K-feldspar. For igneous rocks, F_{cf} and V_P are negatively correlated with the grain size of the major minerals, while T_{cf} is positively correlated. N-A shows a larger D_3 value compared to N-G and N–C, which may result from the interaction of other mineral components. In contrast, for sedimentary rocks, F_{cf} increases with the grain size of the major minerals, while T_{cf} and D_3 decrease. The correlation between V_P and grain size is not significant. Notably, T_{cf} and D_3 exhibit synchronous variation with the grain size, and their relationship with the mineral composition is synergistic, indicating that T_{cf} can serve as an indicator for characterizing the degree of rock damage.
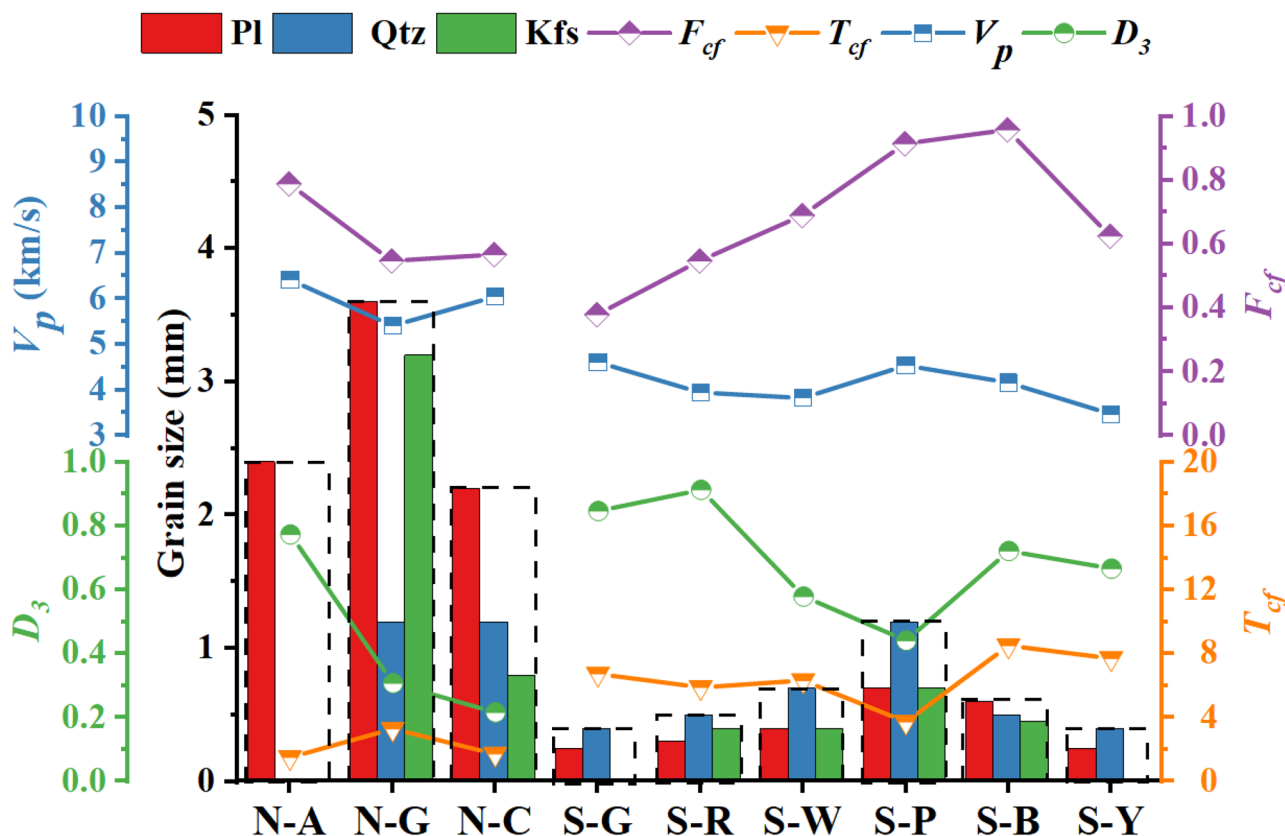

Fig. 11 Relationship between grain size and ultrasonic characteristics, damage

Effect of mineral composition on acoustic properties

In order to investigate the influence of the main mineral components of the rocks (i.e., plagioclase, quartz, and K-feldspar) on F_{cf}, T_{cf}, V_P, and D_3, the relationship between the percentages of the three mineral components and the four parameters was plotted, as shown in Fig. 12. The results demonstrate that F_{cf} exhibits a trend of initially increasing and then decreasing with the increasing content of plagioclase and K-feldspar. With the increase in quartz content, F_{cf} shows high values around 30% and low values around 60%, displaying a bimodal waveform. On the other hand, T_{cf} decreases with increasing plagioclase content, increases with increasing quartz content, and initially increases and then decreases with the increasing content of K-feldspar.

V_P and D_3 exhibit an opposite trend with increasing content of the three mineral components, while the variation pattern of D_3 is the same as that of T_{cf}. These results suggest that the ultrasonic signal characteristics (i.e., T_{cf} and V_P) can effectively reflect the damage characteristics of different rocks.

Discussion

Analysis of the relationship between the lithogenesis and F_{cf}, T_{cf}

It has been concluded from the analysis in the previous section that different types of rock samples exhibit

varying damage evolution trends and ultrasonic signal characteristics under loading, which are closely related to the lithological differences between rocks. Consequently, the rocks in this study were categorized into three groups based on their genetic classification: magmatic, sedimentary, and metamorphic.

Figure 13 displays the increased percentage of F_{cf} and T_{cf} for three types of rock at σ_c. The change rules of F_{cf} and T_{cf} in S-Y are not discussed in this section as it has negative F_{cf}. The dotted lines in the figure represent the average values. The results indicate that lithology affects the increased percentages of F_{cf} and T_{cf}. Metamorphic rocks exhibit the largest increases in F_{cf} and T_{cf}, followed by sedimentary rocks, and magmatic rocks exhibit the smallest increase. This finding can be explained by the structural construction of the rocks. Igneous rocks possess a crystalline connection, leading to close grain contact and the formation of a compact structure (Fig. 3a, b). During loading, the deformation of the rock and contact area between grains does not change significantly. In contrast, sedimentary rocks have a cemented structural connection, where grains are held together by low-strength cement (Fig. 3d). Compared to igneous rocks, sedimentary rocks are more susceptible to larger deformation and matrix compression during loading, leading to a decrease in the distance between sensors and the wave impedance between grains and matrix. Therefore, sedimentary rocks generate larger F_{cf} and T_{cf} than igneous rocks. Despite possessing a crystalline connection, metamorphic rocks exhibit large F_{cf} and T_{cf}. Figure 8a shows that the increasing amplitude of V_P of N-M during the compaction stage (0–20%UCS) is
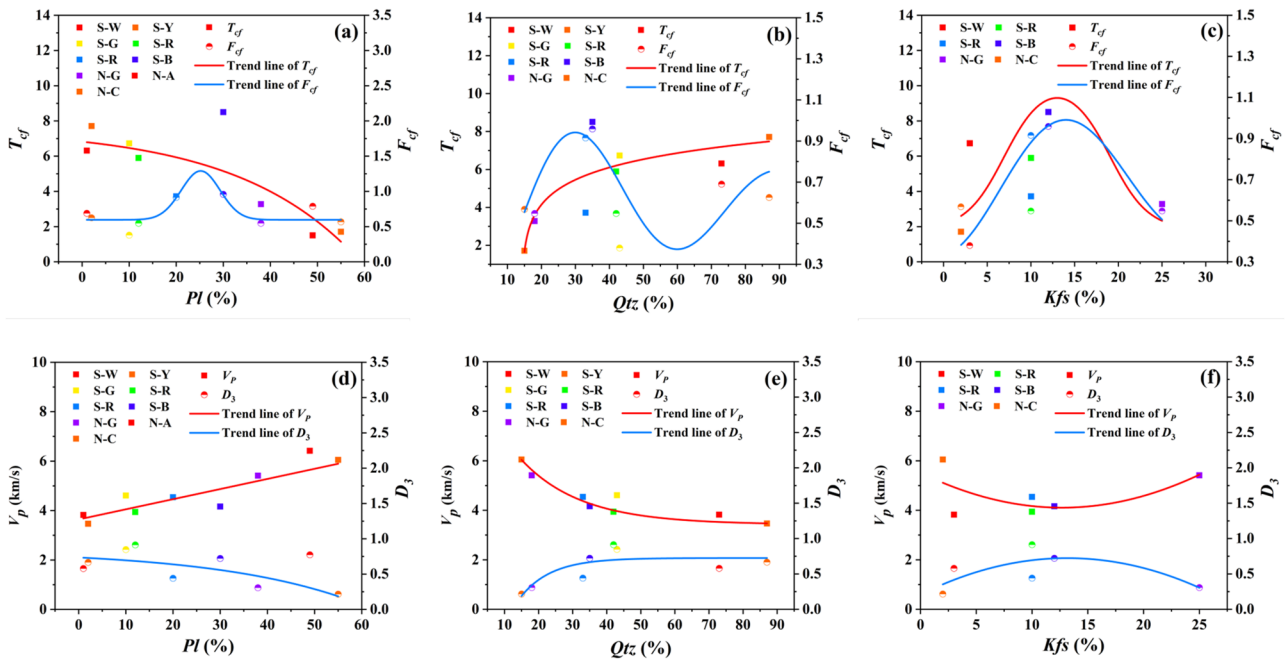

Fig. 12 Relationship between main mineral composition and ultrasonic characteristics, damage **a–c** F_{cf}, and T_{cf} **d–f** V_P and D_3
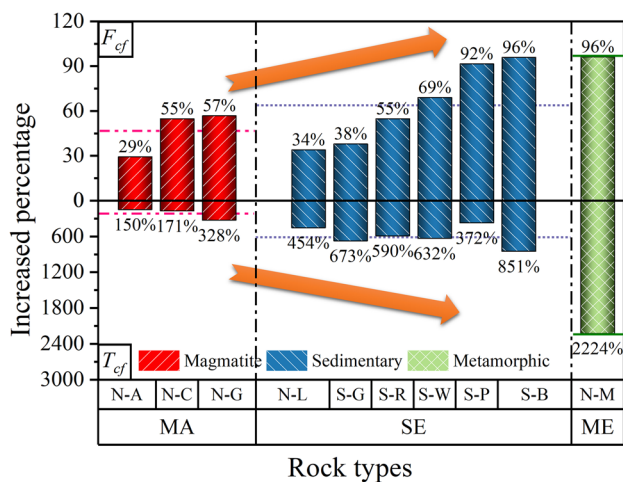
Fig. 13 Increased percentage of F_{cf} and T_{cf} in three classes of rocks

very high, indicating that marble contains an abundance of initial microcracks. The increase in F_{cf} and T_{cf} is attributed to the closure of these microcracks.

Evaluation of rock brittleness

Brittleness is a crucial property of rocks, and its study holds immense significance for stability analysis in rock engineering, classification of blasting, and disaster prevention and control. This section explores the brittleness of different types of rocks based on various brittleness indices and proposes a new method for brittleness assessment using ultrasonic characteristic parameters and mineral content.

Mineral composition exerts a significant influence on the mechanical properties of rocks. It is well known that brittle rocks typically contain a higher proportion of brittle minerals such as quartz, feldspar, and carbonate, while ductile rocks contain lower amounts of these minerals. Therefore, a method

Fig. 14 Evolution trend of brittleness index B_2 with variation of μ

has been proposed to preliminarily assess the brittleness of rocks based on mineral content, which uses the percentage of brittle minerals as an index for brittleness assessment (Liu et al. 2020a, b).

$$B = \frac{W_{qtz} + W_{carb}}{W_{total}} \tag{8}$$

where B stands for brittleness index; W_{qtz} represents the total content of feldspar, quartz, and muscovite; W_{card} represents the content of carbonate minerals (i.e., dolomite, calcite, and other carbonate components); and W_{total} represents the total mineral content.

For rocks of the same type, Eq. (8) can effectively reflect the differences in brittleness between them (Li et al. 2019). However, when comparing rocks with significant differences in lithology, B1 may not be applicable. For instance, according to Eq. (8), the brittleness index of N-G is 0.86 and that of S-Y is 0.90, which is clearly inconsistent with the actual situation that the brittleness of granite is greater than that of sandstone. Therefore, a novel evaluation index was developed to measure the brittleness of different types of rocks, based on the attenuation phenomenon of P-wave velocity propagation in heterogeneous rocks, and considering the response of T_{cf} decline before the UCS (as shown in Fig. 10b, where the higher the brittleness of the rock, the greater the degree of T_{cf} decrease during failure) to the brittleness characteristics of rocks. The brittleness index can be expressed as

$$B_1 = \mu \cdot \zeta \cdot \frac{W_{qtz} + W_{carb}}{W_{total}} + (1 - \mu) \cdot \frac{T_{cf,max}}{T_{cf,p}} \tag{9}$$

$$\zeta = \frac{V_P / \sum_i C_i}{\sum_i C_i \cdot V_{P,i}} \tag{10}$$

where ζ is the reduction factor; μ is the weight coefficient.

In order to select an appropriate value of μ to ensure that the brittle index of granite is greater than that of sandstone, the variation of the brittle index with μ is statistically analyzed for N-G and S-Y. The range of μ values is from 0.5 to 0.95 with an interval of 0.05, as shown in Fig. 14. The brittle index of N-G exceeded that of S-Y at $\mu = 0.9$, so the value of μ in this study is set at 0.9. C_i is the volume fraction of "mineral i"; $V_{P,i}$ is the P-wave velocity of "mineral i" (quartz = 6050 m/s, alkaline feldspar = 5800 m/s, plagioclase = 6250 m/s, calcite = 6681 m/s (Ersoy and Acar 2016)); $T_{cf,p}$ is the value near the UCS; $T_{cf,max}$ is the maximum value generated during the loading. ζ can be interpreted as the degree of attenuation of acoustic energy propagation within the rock. The attenuation phenomenon mainly occurs at the contact
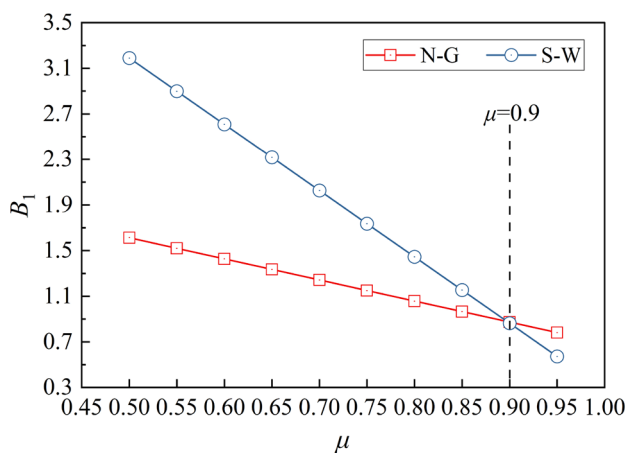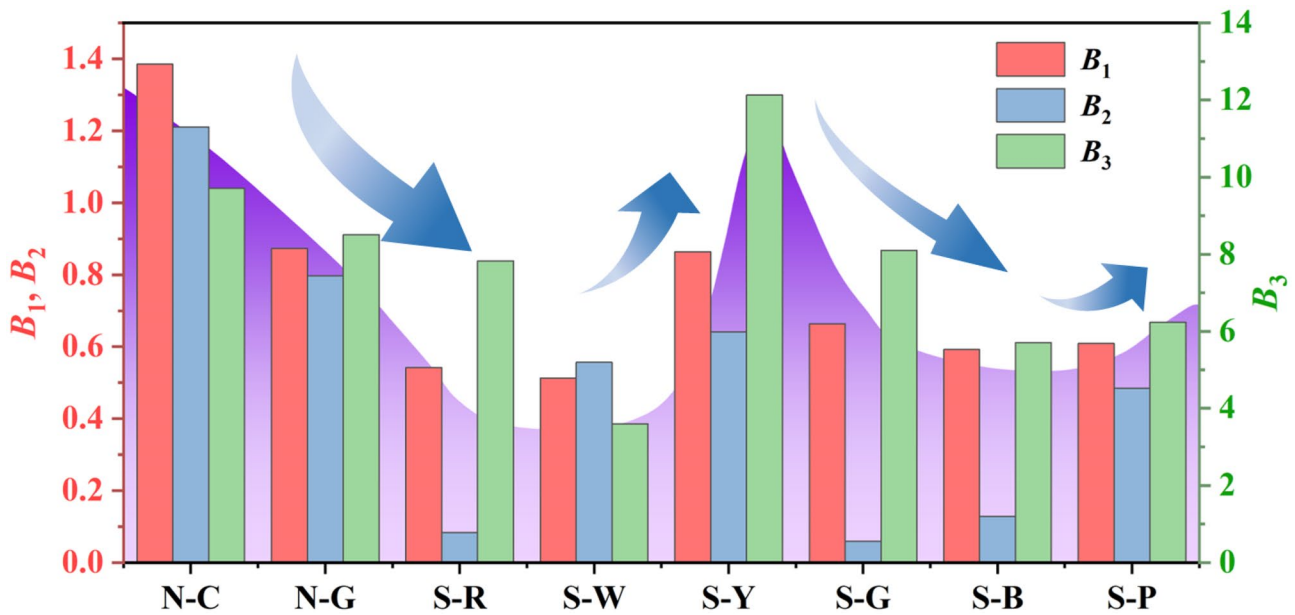
Fig. 15 Comparison of results of different brittleness indexes. B_1, brittleness index based on mineral composition and T_{cf}; B_2, brittleness index based on AE technology; B_3, brittleness index based on stress–strain curve

surfaces of different grains, the contact surfaces between grains and cement, the locations of microcracks, etc. The smaller ζ is, the more events of acoustic energy attenuation occur in these areas.

In order to verify the reliability of the brittleness evaluation method established in this study, two brittleness indexes (B_i) based on stress–strain curve and acoustic emission technology, respectively, were introduced for comparison with B_1. The formula of brittleness indexes is as follows:

$$B_2 = (1 - D_3) \cdot \lg \left[(1 - D_3)/(1 - \sigma_3) \right] \tag{11}$$

$$B_3 = \int_0^{\varepsilon_p} f(\varepsilon)d\varepsilon \Big/ \int_{\varepsilon_p}^{\varepsilon_f} f(\varepsilon)d\varepsilon \tag{12}$$

where D_3 is the damage value at the demarcation points of stages III and IV; σ_3 is the value of the loading percentage corresponding to D_3; $f(\varepsilon)$ is the relation between stress and strain; ε_p is the peak strain in the stress–strain curve; ε_f is the total strain in the stress–strain curve.

B_2 was developed by improving the method established by Hou et al. (2016). Figure 15 presents the results of brittleness evaluation of different rocks obtained by the brittleness indices B_1, B_2, and B_3. It is noteworthy that marble and limestone mainly consist of calcite, and andesite is mainly composed of plagioclase, making their mineral types relatively simple, and thus their brittleness was not evaluated.

The results indicate that the brittleness evaluation results obtained by B_1 are generally consistent with those obtained by B_2 and B_3, especially with B_3 established based on the

aspect of strain energy. Based on the evaluation results of B_1, the brittleness of granite is greater than that of sandstone, and S-Y exhibits the strongest brittleness among sandstones. The order of brittleness evaluation results is as follows: N–C > N-G > S-Y > S-G > S-P > S-B > S-R > S-W.

Conclusions

The acoustic behavior of 11 different rocks under uniaxial compression was studied by ultrasonic and AE testing technology. The effects of grain characteristics and mineral composition on acoustic signal characteristic parameters were discussed from the perspective of microstructure. Finally, a new index for evaluating the brittleness of rock is established based on acoustic characteristic parameters and mineral composition. The following conclusions can be drawn:

1. The increase of wave velocity in sandstone is higher than that in non-sandstone during uniaxial compression, especially at the stage of –20% UCS loading percentage. The damage value at the demarcation points of stages III and IV (D_3) can be used to judge the imminent failure of the rock.

2. Grain uniformity in rocks is quantified using a weighted variable coefficient. F_{cf} and T_{cf} are positively correlated with grain uniformity. Mineral grain size has different effects on igneous and sedimentary rocks. In igneous rocks, grain size is inversely proportional to F_{cf} and V_P, and positively proportional to T_{cf}. In sedimentary rocks,

grain size is positively related to F_{cf} and inversely related to T_{cf} and D_3, but not significantly correlated with V_P.

3. T_{cf} and V_P are negatively correlated with the content of Pl and positively correlated with the content of Qtz, and increase and then decrease with the content of Kfs. F_{cf} increases and then decreases with the content of Pl and Kfs, and the relationship with Qtz shows a bimodal waveform function. The relationship between D_3 and three mineral compositions is contrary to that of T_{cf} and V_P.

4. A novel brittleness index (B_1) based on ultrasonic characteristic parameters and mineral composition is established, and the existing brittleness index is improved to obtain the brittleness index (B_2) calculated based on the damage variables of AE count. The final evaluation results are generally consistent among the three brittle indexes used in this study.

Data availability The data that support the findings of this study are available from the corresponding author, Dr. Tao Zhou, upon reasonable request.

Declarations

Competing interests The authors declare no competing interests.

References

Ajalloeian R, Jamshidi A, Khorasani R (2020) Assessments of ultrasonic pulse velocity and dynamic elastic constants of granitic rocks using petrographic characteristics. Geotech Geol Eng 38(3):2835–2844. https://doi.org/10.1007/s10706-020-01189-6

Atici U (2010) Investigation of ultrasonics sound waves (p and s) behaviour under different pressure for igneous rocks. Int Multidiscip Sci GeoConference: SGEM 1:461–468

Bam L, Miller J, Becker M (2020) A mineral x-ray linear attenuation coefficient tool (MXLAC) to assess mineralogical differentiation for x-ray computed tomography scanning. Minerals 10(5):441. https://doi.org/10.3390/min10050441

Di Martino MDP, De Siena L, Healy D, Vialle S (2021) petro-mineralogical controls on coda attenuation in volcanic rock samples. Geophys J Int 226(3):1858–1872. https://doi.org/10.1093/gji/ggab198

Du K, Li X, Wang S, Tao M, Li G, Wang S (2021) Compression-shear failure properties and acoustic emission (AE) characteristics of rocks in variable angle shear and direct shear tests. Measurement 183:109814. https://doi.org/10.1016/j.measurement.2021.109814

Du K, Sun Y, Zhou J, Khandelwal M, Gong F (2022) Mineral composition and grain size effects on the fracture and acoustic emission (AE) characteristics of rocks under compressive and tensile stress. Rock Mech Rock Eng. https://doi.org/10.1007/s00603-022-02980-y

Ersoy H, Acar S (2016) Influences of petrographic and textural properties on the strength of very strong granitic rocks. Environ Earth Sci 75:1461. https://doi.org/10.1007/s12665-016-6277-y

Gingras MK, MacMillan B, Balcom BJ (2002) Visualizing the internal physical characteristics of carbonate sediments with magnetic resonance imaging and petrography. Bull Can Pet Geol 50(3):363–369. https://doi.org/10.2113/50.3.363

Greenfield RJ, Graham EK (1996) Application of a simple relation for describing wave velocity as a function of pressure in rocks containing microcracks. J Geophys Res Solid Earth 101(B3):5643–5652. https://doi.org/10.1029/95JB03462

Hou P, Gao F, Zhang Z, Yang Y, Teng T (2016) A method for evaluating rock brittleness based on acoustic emission and energy evolution law. J China Univ Min Technol 45(04):702–708. https://doi.org/10.13247/j.cnki.jcumt.000525

Li D, Wei J, Di B, Ding P, Huang S, Shuai D (2018) Experimental study and theoretical interpretation of saturation effect on ultrasonic velocity in tight sandstones under different pressure conditions. Geophys J Int 212(3):2226–2237. https://doi.org/10.1093/gji/ggx536

Li QS, Wang X, Liu J, Xing GZ (2011) Composition and microstructure of a natural nano-structure mineral: six-ring rock. Adv Mater Res 295–297:869–872. https://doi.org/10.4028/www.scientific.net/AMR.295-297.869

Li Z, Deng P, Yang C, Guo Y, Hou L (2019) Evaluation of mechanical properties and compressibility of carbonate reservoir. J Guangxi Univ (Nat Sci Ed) 44(05):1450–1460. https://doi.org/10.13624/j.cnki.issn.1001-7445.2019.1450

Lian Y, Ma Z, Li J, Mou Y, Wang G, Cui J, Fan L (2019) Study on wave velocity variation characteristics of rock during uniaxial loading failure process. Coal Sci Technol 47(08):64–69. https://doi.org/10.13199/j.cnki.cst.2019.08.006

Liu J, Zhang Y, Yang X, Su C (2020a) Experimental study on the uniaxial compression failure and ultrasonic transmission of brittle shale considering the bedding effect. IEEE Access 8:217883–217896

Liu S, Li X, Li Z, Chen P, Yang X, Liu Y (2019) Energy distribution and fractal characterization of acoustic emission (AE) during coal deformation and fracturing. Measurement 136:122–131. https://doi.org/10.1016/j.measurement.2018.12.049

Liu X, Zou D, Liu J, Zhou C, Zheng B (2020b) Experimental study to evaluate the effect of particle size on the small strain shear modulus of coarse-grained soils. Measurement 163:107954. https://doi.org/10.1016/j.measurement.2020.107954

Mayr SI, Burkhardt H (2006) Ultrasonic properties of sedimentary rocks: effect of pressure, saturation, frequency and microcracks. Geophys J Int 164(1):246–258. https://doi.org/10.1111/j.1365-246X.2005.02826.x

Meng Z, Peng S, Fu J (2002) Discussion on controlling factors of rock mechanical properties of coal-bearing rock series. J Rock Mech Eng 01:102–106

Merriam R, Rieke HH, Kim YC (1970) Tensile strength related to mineralogy and texture of some granitic rocks. Eng Geol 4(2):155–160. https://doi.org/10.1016/0013-7952(70)90010-4

Nakagawa S, Nihei KT, Myer LR (2000) Stop-pass behavior of acoustic waves in a 1D fractured system. J Acoust Soc Am 107(1):40–50. https://doi.org/10.1121/1.428292

Ozcelik Y, Bayram F, Yasitli NE (2013) Prediction of engineering properties of rocks from microscopic data. Arab J Geosci 6(10):3651–3668. https://doi.org/10.1007/s12517-012-0625-3

Prikryl R, Lokajicek T, Li C, Rudajev V (2003) Acoustic emission characteristics and failure of uniaxially stressed granitic rocks: the effect of rock fabric. Rock Mech Rock Eng 36(4):255–270. https://doi.org/10.1007/s00603-003-0051-7

Pyrak-Nolte LJ, Myer LR, Cook NGW (1990) Transmission of seismic waves across single natural fractures. J Geophys Res 95(B6):8617. https://doi.org/10.1029/JB095iB06p08617

Quan Y, Harris JM (1997) Seismic attenuation tomography using the frequency shift method. Geophysics 62(3):895–905. https://doi.org/10.1190/1.1444197

Sayers CM (1995) Stress-dependent elastic wave velocities in shales. Int J Rock Mech Min Sci Geomech Abstr 32(3):263–267. https://doi.org/10.1016/0148-9062(94)00049-9

Shirole D, Walton G, Ostrovsky L, Masoumi H, Hedayat A (2018) Non-linear ultrasonic monitoring of damage progression in disparate rocks. Int J Rock Mech Min Sci 111:33–44. https://doi.org/10.1016/j.ijrmms.2018.08.010

Skurtveit E, Torabi A, Gabrielsen RH, Zoback MD (2013) Experimental investigation of deformation mechanisms during shear-enhanced compaction in poorly lithified sandstone and sand: shear-enhanced compaction experiments. J Geophys Res Solid Earth 118(8):4083–4100. https://doi.org/10.1002/jgrb.50342

Tang M, Wang G, Chen S, Yang C (2021) Crack initiation stress of brittle rock with different porosities. Bull Eng Geol Env 80(6):4559–4574. https://doi.org/10.1007/s10064-021-02187-5

Wang S, Liu Y, Du K, Zhou J, Khandelwal M (2020) Waveform features and failure patterns of hollow cylindrical sandstone specimens under repetitive impact and triaxial confinements. Geomech Geophys Geo-Energy Geo-Resour 6(4):57. https://doi.org/10.1007/s40948-020-00183-9

Wang Y, Zhu C, Song ZY, Gong S (2022) Macro-meso failure characteristics of circular cavity-contained granite under unconventional cyclic loads: a lab-scale testing. Measurement 188:110608. https://doi.org/10.1016/j.measurement.2021.110608

Wong LNY, Peng J, Teh CI (2018) Numerical investigation of mineralogical composition effect on strength and micro-cracking behavior of crystalline rocks. J Nat Gas Sci Eng 53:191–203. https://doi.org/10.1016/j.jngse.2018.03.004

Wu Z, Wang Z, Fan L, Weng L, Liu Q (2021) Micro-failure process and failure mechanism of brittle rock under uniaxial compression using continuous real-time wave velocity measurement. J Cent South Univ 28(2):556–571. https://doi.org/10.1007/s11771-021-4621-1

Yang F, Hu D, Zhou H, Lu J (2020a) Physico-mechanical behaviors of granite under coupled static and dynamic cyclic loadings. Rock Mech Rock Eng 53(5):2157–2173. https://doi.org/10.1007/s00603-019-02040-y

Yang H, Duan H, Zhu J (2020b) Effects of filling fluid type and composition and joint orientation on acoustic wave propagation across individual fluid-filled rock joints. Int J Rock Mech Min Sci 128:104248. https://doi.org/10.1016/j.ijrmms.2020.104248

Yang H, Duan HF, Zhu JB (2019) Ultrasonic P-wave propagation through water-filled rock joint: an experimental investigation. J Appl Geophys 169:1–14. https://doi.org/10.1016/j.jappgeo.2019.06.014

Yao Q, Yu L, Li X, Yan K, Xu Q, Wang W, Tang C (2020) The effects of micro- and meso-scale characteristics on the mechanical properties of coal-bearing sandstone. Arab J Geosci 13(17):871. https://doi.org/10.1007/s12517-020-05831-8

Zhang Y, Liu C, Deng H, Lin Y, Li J, Gao F (2022) Peridynamic simulation of heterogeneous rock based on digital image processing and low-field nuclear magnetic resonance imaging. Int J Geomech 22(6):04022083. https://doi.org/10.1061/(ASCE)GM.1943-5622.0002406

Zhao K, Xiong L, Kuang Z, Xu Z, Zeng P (2021) Uniaxial compression creep characteristics and acoustic emission characteristics of two different kinds of red sandstone with different particle sizes. Arab J Sci Eng 46(11):11195–11206. https://doi.org/10.1007/s13369-021-05713-5

Zhao X, Zhou T, Zhai T, Ju Y, Zhu J (2023) Experimental investigation on crack initiation and damage stresses of deep granite under triaxial compression using acoustic methods. J Rock Mech Geotech Eng. https://doi.org/10.1016/j.jrmge.2022.12.035

Zhou T, Chen J, Xie H, Zhou C, Wang F, Zhu J (2022) Failure and mechanical behaviors of sandstone containing a pre-existing flaw under compressive–shear loads: insight from a digital image correlation (DIC) analysis. Rock Mech Rock Eng 55(7):4237–4256

Zhou T, Han D, Zhu J (2023) An experimental study of damage evolution in granite under compression and its influence on wave propagation. Rock Mech Rock Eng. https://doi.org/10.1007/s00603-023-03217-2